COBEM 2023 27TH INTERNATIONAL CONGRESS OF MECHANICAL ENGENEERING

ABCM Brazilian Society of Mechanical Sciences and Engineering
27th ABCM International Congress of Mechanical Engineering
December 04-08, 2023, Florianópolis-SC, Brazil

Relative permeability curves measurement and visualization of pore-scale multiphase flow in fractured porous media

Vivian M. de Sousa
Jorge Avendano
Brenda M. de C. Costa
Marcio S. Carvalho
Pontifical Catholic University of Rio de Janeiro - PUC-Rio
vmendes@lmmp.mec.puc-rio.br
jorge@lmmp.mec.puc-rio.br
brenda@lmmp.mec.puc-rio.br
msc@puc-rio.br

Abstract. *A significant amount of the world's oil and gas reserves come from naturally fractured reservoirs. The heterogeneous nature of this type of formation, including the presence of fractures and vugs, causes the fluid flow to significantly differ from those of conventional reservoirs. Significant progress has been made towards modeling flow in fractured porous media. However, pore-scale phenomena of multiphase flow through the porous matrix embedded with vugs and fractures are still not fully understood. Understanding the flow characteristics at the pore level is necessary to relate macroscopic properties to microscopic displacement mechanisms. The aim of this study is to build relative permeability curves of fractured matrix systems using a microfluidic approach. For this purpose, experimental tests were conducted using PDMS/glass microfluidic devices in order to mimic fractured porous media. Porous media micromodels are widely used to get real-time flow behavior by visualizing in-situ phenomena. They are useful to observe pore scale displacement, investigate a variety of phenomena. The combination of an inverted microscope and a high-speed camera allowed the visualization of the phases' distribution within the porous media. Micrographs taken during the tests provided the necessary information for data analysis. The microfluidic devices were characterized in terms of constriction size distribution, height, porosity, absolute permeability, and pore volume. Two-phase flow tests were conducted to build the relative permeability curves in fractured and non-fractured porous media micromodels. The results indicate that the fractures have a significant effect on the relative permeability curves. Furthermore, in pore scale, fractures connected to a porous matrix show hysteresis effects in both drainage and imbibition processes which are demonstrated on the relative permeability curves.*

Keywords: *fractured porous media, EOR, multiphase flow, microfluidic*

1. INTRODUCTION

Naturally fractured reservoirs constitute a significant portion of the world's hydrocarbon reserves. Some of these reservoirs have been identified as highly productive, despite the heterogeneous nature of this formation type. This heterogeneity, characterized by the presence of fractures, vugs, and interconnected channels, results in a substantially different fluid flow behavior compared to conventional reservoirs.

While significant progress has been made in modeling flow in fractured porous media (Kazemi, 1969; Barenblatt *et al.*, 1960; Pruess and Narasimhan, 1985), the understanding of pore-scale multiphase flow through a porous matrix containing fractures and vugs remains limited. Such understanding is crucial for establishing the relationship between macroscopic properties and microscopic displacement mechanisms. The visualization of fluid behavior in porous media continues to pose a challenge in oil recovery (EOR) studies. In light of this, microfluidic technology has proven to be a suitable approach for addressing this challenge.

Microfluidic micromodels are suitable tool for conducting experimental studies on fluid flow in porous media at the pore scale. They enable the observation, understanding, and identification of several fundamental phenomena occurring within the porous medium. The combination of microscope and microfluidic micromodels facilitate the visualization of phase distribution of fluids within the porous medium (Conn *et al.*, 2014). This capability bridges the gap between microscopic flow dynamics and macroscopic behavior in the porous medium (Tsakiroglou *et al.*, 2003). Consequently, it becomes crucial to examine the relative permeability curves of each phase as a function of saturation under a wide range of experimental conditions.

Tsakiroglou *et al.* (2003) employed glass micromodels to investigate the impact of capillary number on biphasic displacement experiments. The study demonstrated that the relative permeability curves of the two phases are not only

influenced by saturation but also strongly dependent on the capillary number. Alternatively, Chang *et al.* (2009) obtained the relative permeability by maintaining a constant pressure difference between the wetting and non-wetting phases.

Kamari *et al.* (2011) reported the process of miscible displacement in a depleted reservoir. The experiment involved the use of n-heptane to displace n-decane within glass micromodels featuring varying fracture geometries. The authors investigated the influence of a single fracture on the progress of the miscible displacement process. The study revealed that a large fracture length results in a faster advancement of the displacement. Considering the orientation of the fracture, the more directed it was towards the flow, the later the breakthrough was achieved.

Buchgraber *et al.* (2012) described the development and application of a silicon device that exhibits characteristics of double porosity, mimicking systems found in carbonate reservoir rocks. The effectiveness of this micromodel is demonstrated through porosity measurements, examination of displacement mechanisms, determination of recovery factors, and analysis of relative permeability curves.

Kenzhekhanov (2016) utilized a fractured NOA81 micromodel to investigate the impacts of temperature, interfacial tension, and wettability on displacement efficiency. The findings revealed that a partially fractured micromodel exhibited lower production compared to a homogeneous device. However, the fully fractured device did not show any signs of recovery.

Despite previous efforts, there has been a lack of experimental and systematic correlation between the inclusion of fractures with various geometries and distributions within the same porous matrix. Hence, this study aims to examine the fluid dynamics in fractured porous media, comparing different geometries with a reference porous medium without fractures. To achieve this, the microfluidic approach and microscopy techniques are employed to capture images throughout the experiment, enabling the visualization of fluid behavior and the collection of saturation within the device, consequently the construction of relative permeability curves.

2. METHODOLOGY

2.1 Micromodels design and fabrication

The geometries of the porous medium were generated using a pre-designed standard drawing in CAD software, as illustrated in Figure 1.

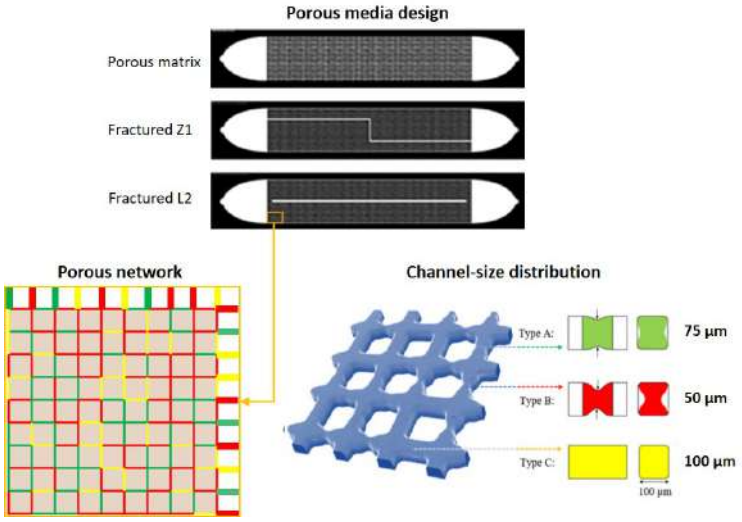

Figure 1. Design of the micromodels using CAD software, distribution of the pore network, size of the constrictions and design of the pillars of the porous medium.

The standard geometry, referred to as the porous matrix, comprises a network of interconnected pores and capillaries, with some possessing throats. To represent this porous medium, open channels made of polydimethylsiloxane (PDMS) were sealed with a glass surface. The PDMS device was fabricated through photolithography, incorporating a 3 mm x 3 mm cell with a network of 10 x 10 interconnected microcapillaries. This design was repeated throughout the micromodel, resulting in a total of 6400 capillaries. All channels exhibit a square profile, approximately 100 μm deep x 100 μm wide, and feature randomly distributed constrictions of sizes 50 μm, 75 μm and 100 μm.

To enhance fluid distribution within the pore network, the model incorporates two regions with ellipsoidal cross-sections, located at the injection and production zones, where fluids are introduced and extracted, respectively. These regions facilitate the accumulation and dispersion of fluids within the pore network. To simulate different fractured media, rows of pillars were selectively removed from the standard geometry, creating a medium with double porosity.

Once the geometries were created in CAD software, the designs were printed onto a photolithography, and a mold of

the micromodel was produced using the soft lithography technique (Xia and Whitesides, 1998). The fabrication process of microfluidic devices using soft lithography involves five key steps: designing the porous medium, printing the mask or photolithography, creating the SU-8 mold, replicating the mold using PDMS, and sealing the PDMS/glass surfaces by oxygen plasma as shown in Figure 2.

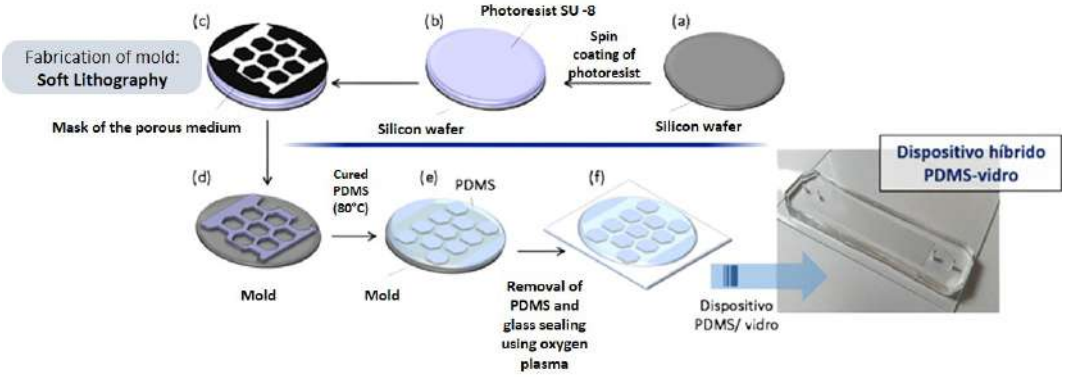

Figure 2. Scheme for obtaining microfluidic devices using the soft lithography technique.

In summary, a silicon wafer surface (Figure 2.a) is uniformly coated with a photoresist SU-8 2025 film using the spin coating technique (Figure 2.b). The pre-designed geometry, created in CAD software and printed onto the photolithography mask, is a template for transferring the microchannel pattern onto the photoresist (Figure 2.c). This transfer is achieved through UV radiation exposure, employing the photolithography process to create the mold (Figure 2.d). The printed geometry on the photolithography mask acts as a barrier, blocking UV light from reaching specific areas of the photoresist and preventing polymerization in those regions.

Following that, the PDMS polymer (Sylgard 184 Elastomer kit, Dow Corning, Germany) is mixed with the curing agent in a ratio of 1:10. The mixture is then placed under vacuum to remove any air bubbles and poured over the mold. The PDMS mixture is subsequently placed in an oven at a temperature of 80°C for approximately 2 hours to initiate the polymerization process and allow the PDMS to solidify. During this step, the microdevice structure within the mold is transferred to the PDMS material . Once solidified, the PDMS is carefully detached from the mold, shaped according to the desired specifications, and opened at designated points to serve as inlet and outlet ports for fluids. Finally, cleaning is conducted using Scoth^{TM} tape to eliminate any traces of dust or dirt from the PDMS microdevice (Figure 2.e).

In the final step, the microfluidic device is sealed using a glass slide to enable microscopy observations. The sealing procedure involves subjecting the device to oxygen plasma treatment (0.5 Torr, 30W) for a duration of 2 minutes. This treatment is carried out utilizing a plasma cleaner (PDC-001, Harrick Plasma, USA) (Figure 2.f).

The devices carried hybrid wettability characteristics due to the inherent hydrophobic nature of PDMS and the hydrophilicity of glass. The application of oxygen plasma treatment during the sealing process facilitates the temporary hydrophilization of the PDMS walls, rendering them hydrophilic for approximately 6 hours (Tan *et al.*, 2010).

2.2 Microfluidic characterization

2.2.1 Dimensions, porosity and channel-size distribution

The micromodels containing fractures and porous matrix were characterized based on their distribution of constrictions, height, porosity, absolute permeability, and pore volume. The devices were saturated with a Drakeol® 7 and Oil glo® 33 oil solution. The SP8 Confocal microscope (Leica Microsystems) was utilized as a microscopy technique to visualize the porous medium and capture images of the devices. After processing the porous medium images, the size distribution and constrictions from the porous medium were determined. Additionally, measurements of the porous volume (V_{pm}) and total volume (V_T) were conducted as means to calculate the porosity ($\varphi = V_{pm}/V_T$).

2.2.2 Absolute permeability measurement

The absolute permeability (K_{abs}) of the micromodels was calculated based on single-phase Darcy's Law (Eq.1).

$$K_{abs} = \frac{L}{A}\mu\frac{Q}{\Delta P} \tag{1}$$

For this purpose, pressure drop across the porous media (ΔP) was measured during the flow of Drakeol® 7 and Oil glo® 33 oil solution with a specific (μ) fluid viscosity at several flow rates (Q) in a range from 0.5 cc/h to 2 cc/h through the porous medium. A micromodel with a determined length (L), cross-sectional area (A) was used during the experiments.

Initially, the devices were completely saturated with the oil solution using a single-syringe pump (Harvard Apparatus Elite 11 model), connected to the micromodel inlet port through tubing. For each flow rate injected within the range of 0.5 cc/h to 2 cc/h, the pressure drop across the porous media was measured. This was accomplished by utilizing two pressure transducers connected to the porous medium: a 15 psi transducer at the inlet (Velki) and a 1.5 psi transducer at the outlet (WIKA). The absolute permeability was calculated as an average of three independent experiments.

2.2.3 Relative permeability measurements

Relative permeability curves were obtained using two fluids: Drakeol® 7 and Oil-Glo 33® (0.1%), and MilliQ® water and methylene blue (1.2%). The micromodel was initially saturated with the oil phase, then the process of simultaneous injection of the two phases was started at a constant total flow rate of 2 cc/h (Q_T). In each run, the water fraction flow rate $(fw = Q_w/Q_T)$ was varied from 1 to 0, covering a total of 11 points on the relative permeability curve. Once a steady-state flow regime was achieved, pressure readings and image acquisition were performed to observe the phase distribution within the micromodel. The saturation of water and oil within the porous medium was quantified through image processing using ImageJ® software.

By utilizing Equation 2, which is based on Darcy's law, we can determine the effective permeability (K_{eff}) of each phase by considering the injection flow rate (Q_i) and the steady-state pressure drop (ΔP). The relative permeability is then calculated as the ratio between the effective permeability and the absolute permeability of the porous media (K_{abs}).

$$K_{eff} = \frac{L}{A}\mu_i \frac{Q_i}{\Delta P} \tag{2}$$

where the subscript *i* refers to the phase *i*.

2.2.4 Velocity test

The velocity test was conducted to investigate the impact of different injection rates on porous media invasion, both with and without fractures. The tests involved the use of Drakeol® 7 with Oil-Glo 33® (0.1%) oil and MilliQ® water with methylene blue (1.2%). Initially, three devices of each geometry, porous matrix and Z1 fracture were saturated with the oil phase.

Once the devices were saturated, the injection process with water at several velocities was carried out following three protocols, as shown in Figure 3. Upon reaching a steady-state condition in terms of pressure drop, pressure readings were recorded, and images were captured.

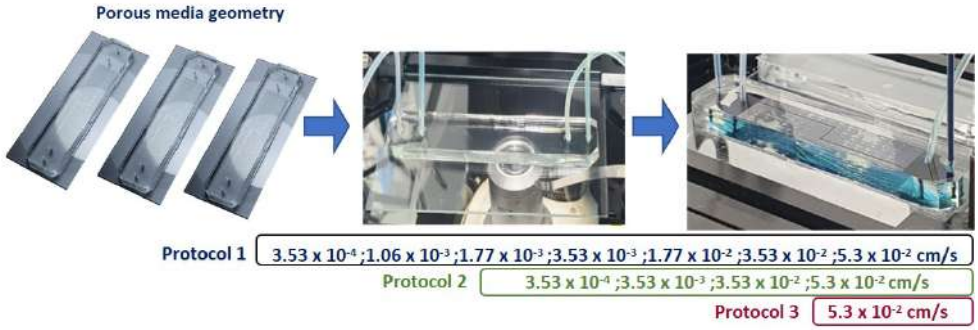

Figure 3. Experimental procedure used in the velocity test. (a) Device saturate with oil (b) Drainage with water at various speeds following three protocols.

3. Results and Discussion

3.1 Micromodel characterization

3.1.1 Dimensions of the device

The devices shared the same dimensions in terms of length and width, measuring 4.8 cm and 1.18 cm, respectively. Height measurements were acquired using microscopy. Table 1 provides a summary of the dimensions of the micromodels' porous medium, including the cross-sectional area in the injection/production zones. Details of throat distributions found for the porous matrix and fractured devices are shown in Figure 4.

Table 1. Dimensions of the micromodels' porous medium.

	Porous Matrix	**Fractured Z1**	**Fractured L2**
Height , H (μm)	91.50	89	90.60
Lenght, L (cm)	4.8	4.8	4.8
Width, W (cm)	1.18	1.18	1.18
Area, A (cm^2)	1.08×10^{-2}	1.05×10^{-2}	1.07×10^{-2}
Throats size (μm)	21-101	21-101	21-101
Fracture width (μm)	-	320-379	620-669

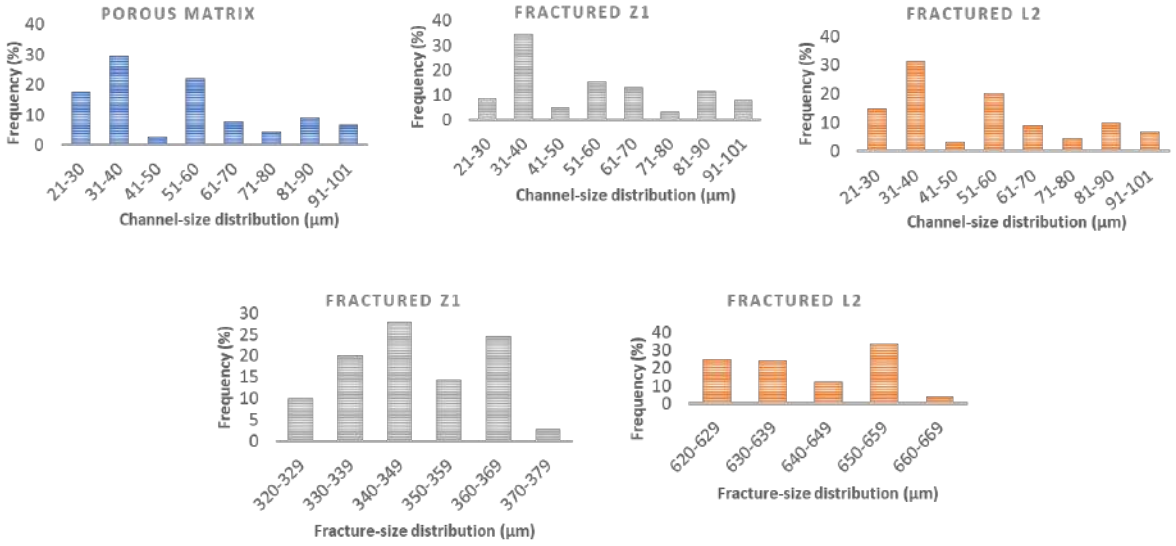

Figure 4. Throats and fracture size distribution of PDMS/glass devices.

The porous matrix of the devices was designed to include channels with widths of 50 μm, 75 μm and 100 μm. Throat sizes range from 21 μm to 101 μm in width, with distribution of modal values being 31-40 μm, 51-60 μm, and 81-90 μm for the three devices. The distribution of throat sizes observed in the non-fractured device was similar to that found in the porous medium of the fractured devices. Therefore, the results obtained from the devices with and without fractures will elucidate the impact of the fracture at fluid behavior.

3.1.2 Absolute Permeability

According with Darcy's Law, the absolute permeability can be obtained directly by the angular coefficient of the curves, which correlates the pressure drop with a single-phase fluid flow rates, taking into account the dimensions of the porous medium (Table 1) and the viscosity (μ) of Drakeol ® 20.39 cP (22°C) The values achieved were 24.5 D, 59.7 D and 63.2 D for porous matrix, Z1 fracture and L2 fracture, respectively. As expected, the absolute permeability values for the fractured media were at least two times higher than the porous matrix.

3.1.3 Macroporosity

Using the dimensions of the device and data obtained from image processing, we calculated the total volume and the porous volume of the micromodel. With these data, the macroporosity of porous media can be obtained. Therefore, we have $\varphi = 48\%$ to non-fractured porous media, $\varphi = 50\%$ to fractured Z1 and $\varphi = 51\%$ to fractured L2. The internal volume of the porous media was calculated resulting in V_{pm} = 24, 25 and 25 μl to porous matrix, fractured Z1 and fractured L2, respectively.

3.2 Velocity test

The Figure 5 displays images of the porous matrix micromodel after injecting water in a several flow rates according to three velocity-based protocols. We observed that the experiment following protocol 1 exhibited lower oil ganglia compared to protocols 2 and 3. However, the water saturation within the devices with the same flow rate remained unaffected by the protocol used. This indicated that the initial condition does not influence water saturation in the porous matrix. On the other hand, the initial condition determined the number of oil ganglia into the system.

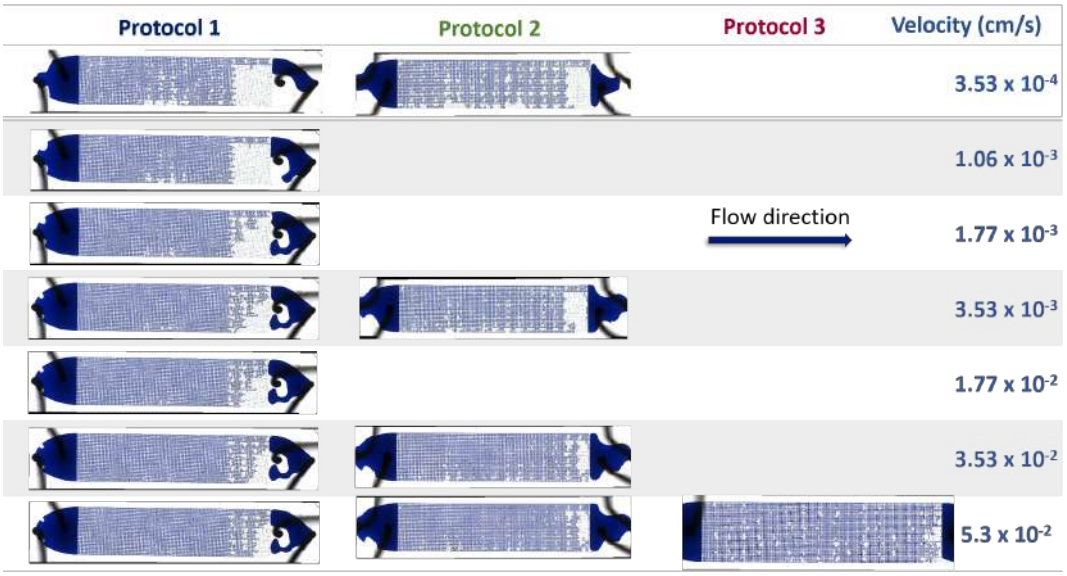

Figure 5. Porous matrix micromodels used in the velocity tests following Protocol 1, Protocol 2 and Protocol 3. Aqueous phase is in blue and oil phase is in white.

The experiment with the Z1 fracture followed the same procedure as the test with the porous matrix. As seen in Figure 6 a notable difference in water saturation within the device was observed. This divergence in water saturation was particularly notable when comparing protocol 1 with protocol 3, highlighting the significant influence of the initial experimental condition in fractured systems.

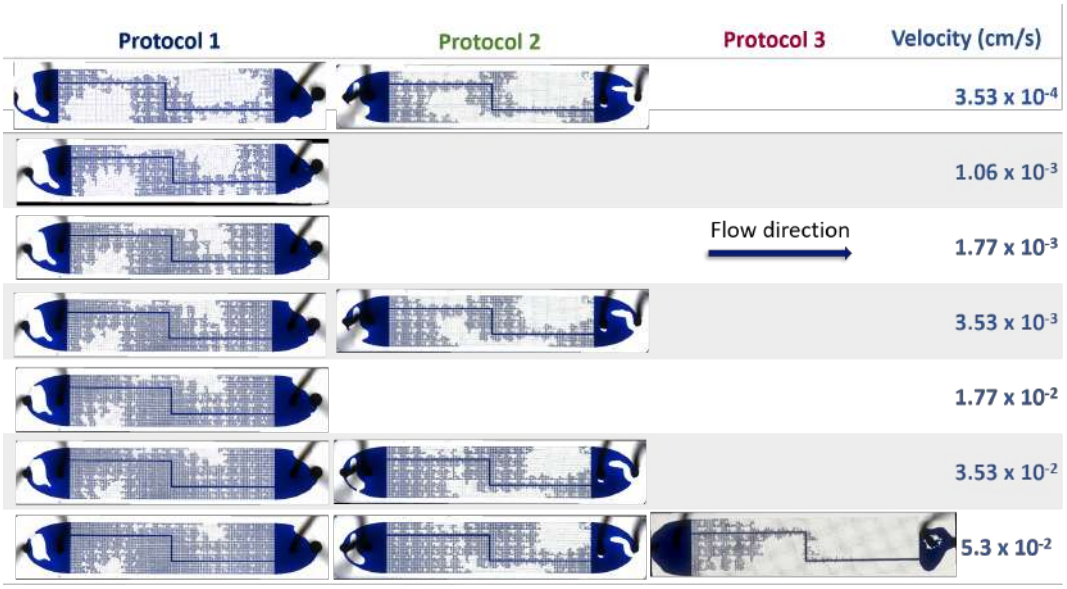

Figure 6. Fractured micromodels employed in velocity tests following Protocol 1, Protocol 2 and Protocol 3. Aqueous phase is in blue and oil phase in white.

To enhance our understanding of the system, water saturation was quantified in both porous matrix and Z1 geometry devices.

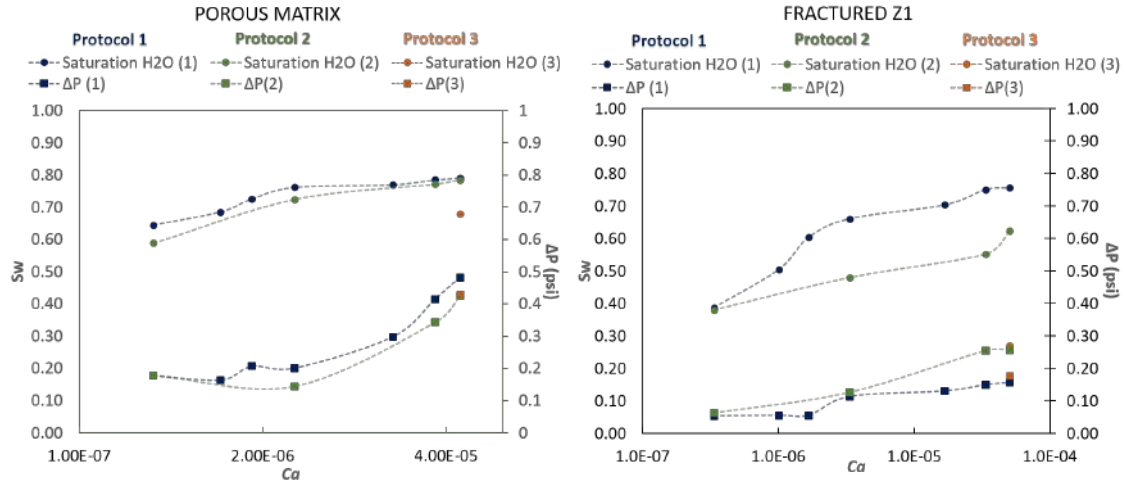

Figure 7. Velocity test curves correlating water saturation and pressure drop with system capillary number variation for Z1 fracture and porous matrix devices.

The Figure 7 illustrates the difference between the results obtained from protocol 1 and protocol 2 in terms of water saturation within the device and pressure drop values (ΔP). In the fractured micromodel Z1, a notable contrast between the protocols is observed, with a difference of 38% in water saturation and 70% in ΔP. Conversely, when considering the porous matrix, there were no significant variations in water saturation values between protocols, with a maximum difference of 9%. Additionally, higher ΔP values were measured for the non-fractured device in comparison to the fractured device, which aligns with expectations since the presence of the fracture increase the permeability of the porous medium.

3.3 Relative permeability measurements

Relative permeability curves provides a series of information of the analyzed porous medium. A better understanding of fluid behavior in the porous medium and also to measure the impact of the fracture on fluid flow. As mentioned before, the relative permeability was determined using Darcy's law. For the construction of the relative permeability curves, during the steady state in the pressure drop, images of the device were acquired in the simultaneous two-phase flow at a constant total flow rate of 2 cc/h. In each run, the water fraction flow rate (f_w) varied from 1 to 0 as shown in Figure 8.

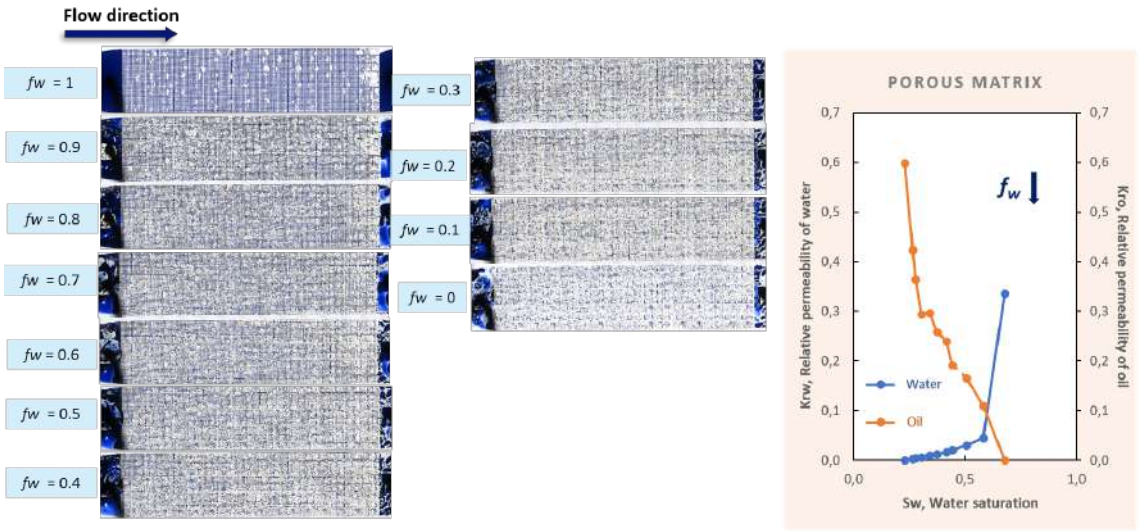

Figure 8. Simultaneous two-phase flow and relative permeability curves obtained for the porous matrix micromodel. Water fraction flow rate varying from 1 to 0. The water is blue and the oil is white.

As evidenced by the micromodel images captured under the microscope, we observed as the water fraction flow rate decreases, the water saturation within devices decreases. Correlating the water saturation with relative permeability values, we plotted the relative permeability curves for water and oil, as shown in Figure 8.

The relative permeability curves exhibit a similar trend, the water permeability proportionally decreases with wa-

ter saturation, consequently the hydrophobic device demonstrated a higher permeability for a wetting phase (60%). In addition, we achieved a residual oil saturation ($S_{or} = 0.32$).

Regarding the fractured micromodel Z1, we performed the same experiment. In order to obtain the relative permeability curves, during the steady state in the pressure drop, images of the device were acquired in the simultaneous two-phase injection at a constant total flow rate of 2 cc/h in Z1 fractured micromodel. In each run, the water fraction flow rate (f_w) varied from 1 to 0 as shown in Figure 9

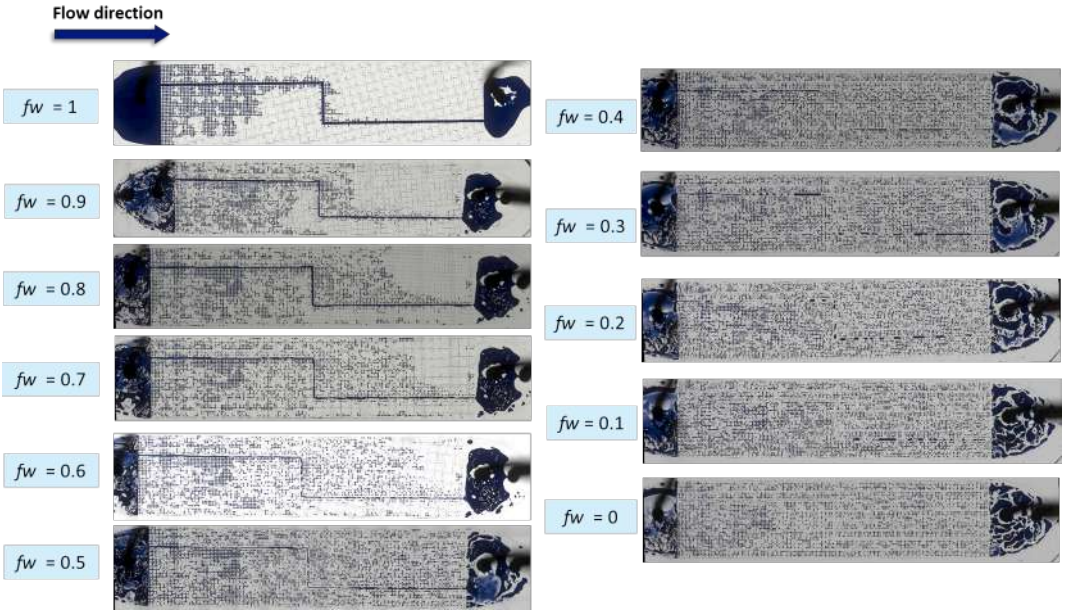

Figure 9. Simultaneous two-phase flow in Z1 fractured micromodel.Water fraction flow rate varying from 1 to 0. The water is blue and the oil is white.

Correlating the water saturation within the fractured device with relative permeability values, we obtain the relative permeability curves for water and oil as shown in Figure 10.

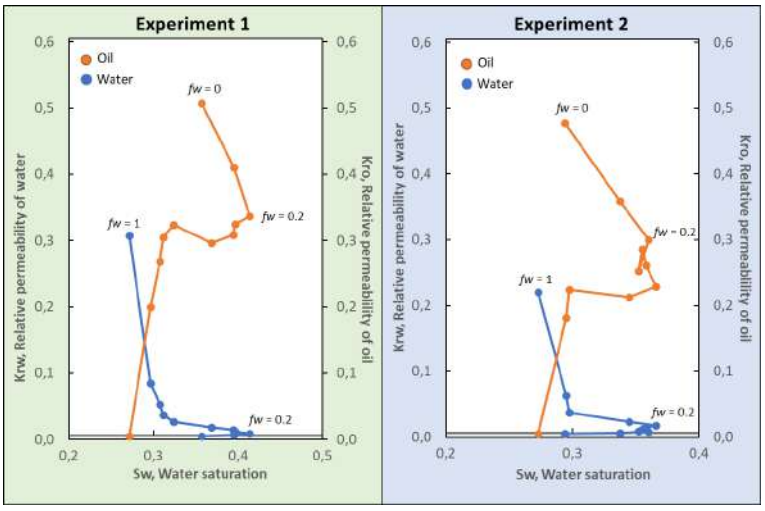

Figure 10. Relative permeability curves obtained from duplicate experiments for the Z1 fractured micromodel.

In the study of fractured porous media, despite a decrease in water fraction (f_w), an increase in water saturation within the device is observed. During water injection ($f_w = 1$), fractures become the preferred pathway, permeating only 20% in the porous matrix.

Additionally, a sudden decline in the relative permeability of water, accompanied by an increase in the relative permeability of oil, is noted up until $f_w = 0.5$. At this point, we visualized water throughout the porous medium, and thereafter, the relative permeability values remain relatively constant until $f_w = 0.2$. At $f_w = 0.2$, the fracture, previously predominantly filled with water, begins to be invaded by oil, becoming the preferred pathway for oil flow. Consequently, the water saturation within the fractured device decreases while there is a significant increase in the relative permeability of oil. To

confirm the results, a duplicate experiment was conducted, yielding similar results according to the graphics in the figure Figure 10.

3.3.1 Relative permeability measurements - Hysteresis

Upon analyzing the results of the fractured micromodel experiment, it was evident that further tests were required to investigate the hysteresis effect in this system and gain a deeper understanding of fluid behavior in fractured porous media. Hysteresis effect is often observed due to capillary forces and fluid-fluid interactions within the pores. Thus, experiments were conducted where the water fraction flow rate followed the reverse path of the previous tests. In other words, the water fraction flow rate was varied from 0 to 1 (Figure 11). The experimental setup and procedures remained consistent, but the water fraction rate increased throughout the experiment while the oil injection rate decreased. Two tests were conducted using the same geometry, as depicted in Figure 12.

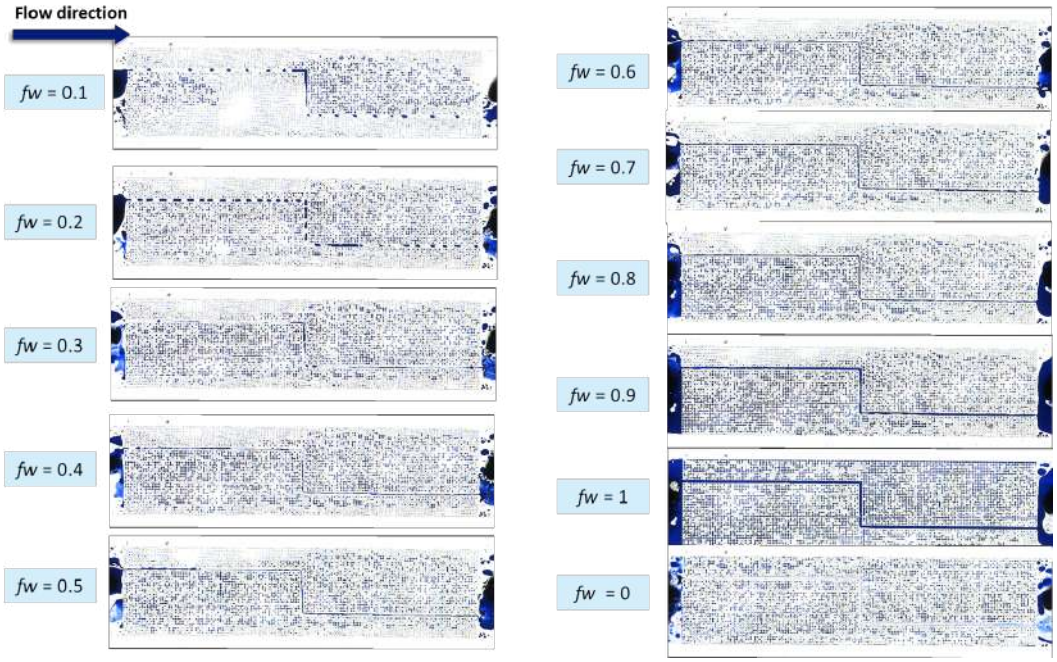

Figure 11. Hysteresis test for the Z1 fractured micromodel. Water fraction flow rate varying from 0 to 1. The water is blue and the oil is white.

In the images above it has been observed that as the water fraction flow increases the water saturation also increases.

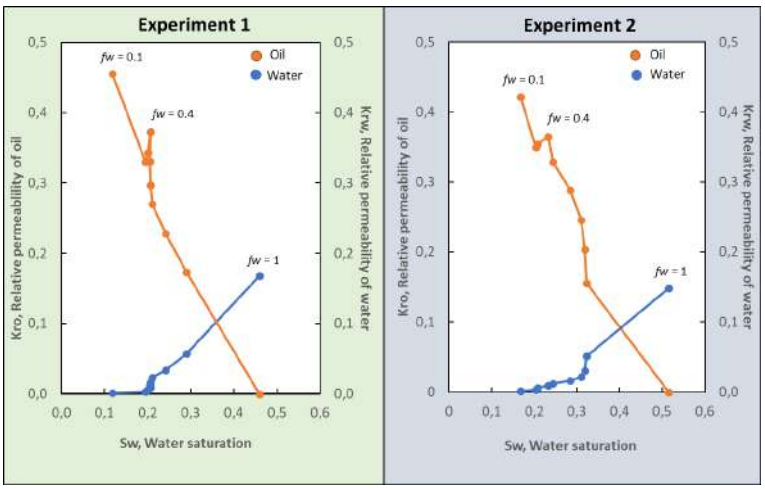

Figure 12. Relative permeability curves obtained from hysteresis test for the Z1 fractured micromodel. Water fraction flow rate varying from 0 to 1.

The relative permeability curves obtained from hysteresis test for the fractured devices exhibited a profile remarkably differ to those acquired with previous tests. This confirmation validated the occurrence of hysteresis within this system

with double porosity, meaning that the flow properties differ during the drainage and imbibition processes.

4. CONCLUSIONS

The utilization of microfluidic devices equipped with an optical window allows for the identification of anomalies occurring during fluid flow in fractured porous media. This approach enables simultaneous visual monitoring of phenomena and pressure measurements, which cannot be achieved with other strategies like core flooding.

In summary, the analysis of the results demonstrates that the presence of fractures in a porous medium leads to unconventional behavior during multiphase flow. Velocity tests indicate that the initial experimental conditions significantly influence the saturation and pressure drop values in fractured systems. The proximity of fractures to the porous matrix induces an antagonistic displacement effect, which differs from the behavior observed in systems consisting solely of the porous matrix. The relative permeability curves obtained from the fractured Z1 device further highlight the importance of the initial experimental conditions in generating informative data throughout the test. Moreover, the presence of fractures creates preferential pathways for the fluids, altering the expected relationship between saturation within the device and the water fractional flow rate.

These experiments demonstrate significant potential, as there are currently no studies reporting this anomalous behavior in fractured media for relative permeability investigations. The results presented here are relevant not only for the academic community but also for modeling and simulation efforts.

5. REFERENCES

Barenblatt, G.I., Zheltov, I.P. and Kochina, I., 1960. "Basic concepts in the theory of seepage of homogeneous liquids in fissured rocks [strata]". *Journal of applied mathematics and mechanics*, Vol. 24, No. 5, pp. 1286–1303.

Buchgraber, M., Al-Dossary, M., Ross, C. and Kovscek, A.R., 2012. "Creation of a dual-porosity micromodel for pore-level visualization of multiphase flow". *Journal of Petroleum Science and Engineering*, Vol. 86, pp. 27–38.

Chang, L.C., Chen, H.H., Shan, H.Y. and Tsai, J.P., 2009. "Effect of connectivity and wettability on the relative permeability of napls". *Environmental geology*, Vol. 56, pp. 1437–1447.

Conn, C.A., Ma, K., Hirasaki, G.J. and Biswal, S.L., 2014. "Visualizing oil displacement with foam in a microfluidic device with permeability contrast". *Lab on a Chip*, Vol. 14, No. 20, pp. 3968–3977.

Kamari, E., Rashtchian, D. and Shadizadeh, S.R., 2011. "Micro-model experimental study of fracture geometrical effect on breakthrough time in miscible displacement process".

Kazemi, H., 1969. "Pressure transient analysis of naturally fractured reservoirs with uniform fracture distribution". *Society of petroleum engineers Journal*, Vol. 9, No. 04, pp. 451–462.

Kenzhekhanov, S., 2016. *Chemical EOR process visualization using NOA81 micromodels*. Colorado School of Mines.

Pruess, K. and Narasimhan, T., 1985. "A practical method for modeling fluid and heat flow in fractured porous media". *Society of Petroleum Engineers Journal*, Vol. 25, No. 01, pp. 14–26.

Tan, S.H., Nguyen, N.T., Chua, Y.C. and Kang, T.G., 2010. "Oxygen plasma treatment for reducing hydrophobicity of a sealed polydimethylsiloxane microchannel". *Biomicrofluidics*, Vol. 4, No. 3, p. 032204.

Tsakiroglou, C., Theodoropoulou, M., Karoutsos, V., Papanicolaou, D. and Sygouni, V., 2003. "Experimental study of the immiscible displacement of shear-thinning fluids in pore networks". *Journal of colloid and interface science*, Vol. 267, No. 1, pp. 217–232.

Xia, Y. and Whitesides, G.M., 1998. "Soft lithography". *Annual review of materials science*, Vol. 28, No. 1, pp. 153–184.